The Dielectric Cavity Antenna - An Alternative to the Choke Ring Antenna

Frank N. Bauregger, Todd Walter, and Per Enge,
Department of Aeronautics and Astronautics, Stanford University

Biography

Frank N. Bauregger is a Ph.D. candidate in the Electrical Engineering Department at Stanford University. He received his B.S. in Electrical Engineering from the Pennsylvania State University. His research focuses on the design of interference resistant antennas for airborne GPS applications.

Todd Walter, Ph.D, is a research associate in the Department of Aeronautics and Astronautics at Stanford University. Dr. Walter received his Ph.D. in 1993 from Stanford and is currently developing WAAS integrity algorithms and analyzing the availability of the WAAS signal.

Per Enge, Ph.D., is professor of Aeronautics and Astronautics at Stanford University. A Ph.D. graduate of the University of Illinois, his research focuses on WAAS and LAAS aircraft landing applications.

Abstract

Antennas for airborne GPS applications would ideally have a radiation pattern which is uniform for elevation angles greater than 5°, and which has zero gain for angles below. Such an antenna would be immune to radio frequency interference (RFI) originating from below the aircraft, but would still provide coverage for low elevation GPS satellites. Though not ideal, choke ring antennas reject multipath and interference very well. Unfortunately, choke ring antennas cannot be used for airborne applications due to their large size. This paper describes an interesting type of interference resistant antenna which is a variation of the choke ring. It resembles a choke ring antenna, but instead of a corrugated surface, its ground plane is a single cavity filled with dielectric material. The cavity is sized such that the transverse magnetic field at the surface vanishes, resulting in an artificially soft surface for TM waves. This novel ground plane and its associated patch antenna source are collectively called the dielectric cavity antenna (DCA).

The DCA is analyzed using a 2.5-dimensional finite difference time domain (FD-TD) technique. In this method, all field components are assumed to obey a $\cos\phi$ or $\sin\phi$ variation, thus obviating the need for a full three-dimensional analysis. The radiating source for the DCA is a nearly-square microstrip patch antenna, which is approximately modeled by a circumferential magnetic line current, obeying a $\cos\phi$ variation.

A prototype DCA has been built and tested. During the fabrication process, the dielectric material used for the prototype DCA became filled with a small amount of trapped air, unexpectedly lowering the effective permittivity of the dielectric. This effect was observed as a deviation from the expected radiation pattern, but was subsequently predicted by the FD-TD algorithm by artificially reducing the permittivity of the cavity. While the prototype DCA exhibits high zenith gain, it attenuates signals near the horizon severely. When the proper dielectric is used, the performance of the DCA is nearly identical to that of a choke ring antenna. Smaller, airworthy versions of the DCA may be built if suitable, high-permittivity materials are used in the cavity.

1. Introduction

The recent growth of wireless communication services, and the possible implementation of ultra-wideband (UWB) data systems have heightened the concern for unintentional interference to GPS for airborne users. Intentional jamming poses an additional threat to the availability of GPS for airborne navigation. These concerns warrant the development of a specialized interference resistant antenna which ideally has a uniform radiation pattern for elevation angles greater than 5°, and no response below. Toward that end, this paper describes the design, analysis, and test results of the dielectric cavity antenna (DCA). This antenna is similar to a choke ring antenna in that it uses an artificially soft surface to minimize sensitivity to signals arriving from below the

horizon. However, the soft surface is realized with a dielectric cavity instead of a corrugated ground plane.

The DCA is analyzed using the finite-difference time-domain (FD-TD) method, whereby Maxwell's equations are discretized in space, and solved incrementally in time until steady state conditions are reached. Due to the axial symmetry of the DCA, it is analyzed most readily in cylindrical coordinates. Far-field radiation patterns are obtained by employing the near-to-far-field transformation [1], which simply propagates the equivalent currents on a virtual surface enclosing the antenna to a distant observation point, taken to be in the far-field. The radiation pattern of the DCA is controlled by varying the depth, radial width, and permittivity of the dielectric cavity. When sized properly, the transverse (to the direction of propagation) magnetic field is forced to zero on the cavity surface, thus establishing an artificially soft surface for vertically polarized (TM) waves. The proper dimensions for the resonant cavity are first estimated by treating the cavity as an infinite grounded dielectric slab. The optimum height of the cavity is then simply a function of ϵ_r. The cavity should be an integral number of half-wavelengths long. The final dimensions are determined through repeated iterations of the FD-TD computer code.

A prototype DCA was constructed and tested. Since the dielectric used for the prototype DCA collected trapped air during the fabrication process, the observed radiation pattern was different than expected. However, the experimental radiation pattern can be predicted by the FD-TD algorithm when a slightly lower permittivity is assumed for the dielectric cavity, owing to the trapped air pockets. Two additional antennas were analyzed and tested for comparison purposes – a Novatel 501 GPS antenna with an A031 choke ring ground plane, and a 30 cm diameter circular metal plate fitted with a Trimble airborne patch antenna.

2. Artificially Soft Surfaces

2.1. Definition
An electromagnetic soft surface can be simply defined as any surface on which the transverse (to the direction of propagation) electric and magnetic fields are both forced to zero. This structure will not support the propagation of plane waves along its surface. If either of the above conditions is met separately, the surface will not support the propagation of either horizontally or vertically polarized plane waves, respectively. Expressed another way, a surface is said to be soft for horizontal polarization if

$Z_t = E_t/H_l = 0$, or soft for vertical polarization if $Z_l = -E_l/H_t \to \infty$. Z_t and Z_l are the transverse and longitudinal wave impedances, respectively [2]. As an example, consider a horizontally polarized plane wave traveling along an infinite planar surface. A perfectly electric conducting (PEC) surface will force the tangential electric field E_t to zero, and will thus prevent propagation of the plane wave along the surface. For a vertically polarized plane wave, the soft surface is achieved by instead making the surface a perfect magnetic conductor (PMC), which forces H_t to zero. The fictitious perfect magnetic conductor can be realized artificially by various structures. The most common is the corrugated surface, with the corrugation fins oriented transverse to the direction of propagation, and approximately $\lambda_0/4$ deep. Also, it can be shown that an infinite grounded dielectric slab of thickness $d = \lambda_0/(4\sqrt{\epsilon_r - 1})$ acts as an electromagnetic soft surface [3]. This can be shown by considering the longitudinal wave impedance $Z_l = jk_0\sqrt{\epsilon_r - 1}/(\omega\epsilon)\tan(k_0 d\sqrt{\epsilon_r - 1})$, which approaches infinity when $d \to \lambda_0/(4\sqrt{\epsilon_r - 1})$.

2.2. Previous Research – Dielectric Slab Antennas
The authors in [3] used this concept to design a 5λ diameter circular dielectric slab antenna, identical to the antenna discussed in this paper, except with a vertical monopole as the source of radiation. Both the antenna and the source were axially symmetric, permitting a simplified two-dimensional TM analysis of the antenna. The authors investigated slabs of critical thickness, with and without a PEC termination around the circumference of the slab. The dielectric cavity monopole antenna was built and tested with and without the edge termination, as discussed in [4]. The terminated antenna antenna provided significant suppression of sidelobes below the ground plane. However, at the GPS L1 frequency of 1.575 GHz, this antenna would be over a meter in diameter, clearly too large for practical airborne use. We desire a smaller version of this antenna which may be realized by increasing the permittivity and/or permeability of the dielectric material, thus reducing the critical thickness, and possibly reducing the diameter of the disk.
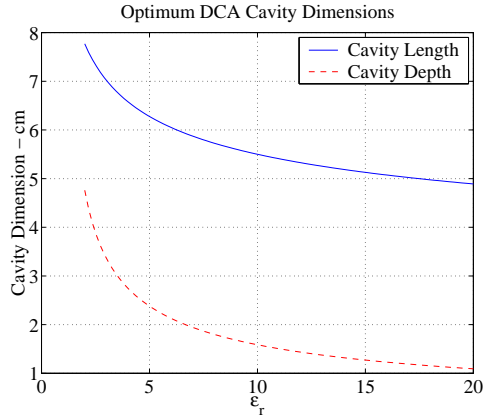
2.3. Optimum Cavity Dimensions
In this section, we discuss a method for estimating the optimum dimensions of the cavity length and depth. We begin by considering the infinite grounded dielectric slab, shown in Fig. 1. Terminating the infinite dielectric slab with vertical PEC sheets will generate standing waves within the slab. There will be periodic nulls of the electromagnetic fields each π/β meters, where β is the propagation constant in the z
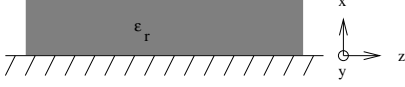
Figure 1: Planar geometry for an infinite grounded dielectric slab.

direction within the slab. For a given dielectric material having relative permittivity ϵ_r, the wavenumber β must be determined on a case basis by solving a transcendental equation obtained by enforcing continuity of the tangential field components at the air-dielectric interface. In order to properly terminate the DCA with vertical PEC sheets, we must ensure that the sheets are placed at E_x field nulls. Using image theory, one can reason that the presence of the sheets will not change the field structure within the slab. From this, we conclude that the optimum length of the cavity is $n\pi/\beta$, with $n = 1, 2, 3, ...$ The optimum cavity depth is, of course, $\lambda_0/(4\sqrt{\epsilon_r - 1})$. Fig. 2 shows these optimum dimensions over a range

Figure 2: Optimum cavity dimensions for the DCA.

of practical ϵ_r. The values plotted in Fig. 2 are ideal, and the actual optimum cavity dimensions will differ. For example, the prototype DCA with $\epsilon_r = 2.37$ was constructed having a cavity length of 9.3 cm, which is greater than a length of 7.5 cm suggested by Fig. 2. Fig. 2 should be used only as a starting point for the design of a DCA. Further iterations of the FD-TD computer code are required before a working antenna can be designed.

3. 2.5-Dimensional FD-TD Algorithm

Performing a full three-dimensional FD-TD analysis for even a small structure is unattractive because of the time required to complete the simulation. It would be much more efficient to take advantage of the axial symmetry of the DCA and employ a two-dimensional code. A procedure for doing this will be briefly described in this section.

First, consider that in cylindrical coordinates, Maxwell's equations are written generally as

$$\frac{1}{\rho}\frac{\partial E_z}{\partial \phi} - \frac{\partial E_\phi}{\partial z} = -\mu\frac{\partial H_\rho}{\partial t} - M_\rho, \tag{1}$$

$$\frac{\partial E_\rho}{\partial z} - \frac{\partial E_z}{\partial \rho} = -\mu\frac{\partial H_\phi}{\partial t} - M_\phi, \tag{2}$$

$$\frac{1}{\rho}\frac{\partial(\rho E_\phi)}{\partial \rho} - \frac{1}{\rho}\frac{\partial E_\rho}{\partial \phi} = -\mu\frac{\partial H_z}{\partial t} - M_z, \tag{3}$$

$$\frac{1}{\rho}\frac{\partial H_z}{\partial \phi} - \frac{\partial H_\phi}{\partial z} = \epsilon\frac{\partial E_\rho}{\partial t} + \sigma E_\rho + J_\rho, \tag{4}$$

$$\frac{\partial H_\rho}{\partial z} - \frac{\partial H_z}{\partial \rho} = \epsilon\frac{\partial E_\phi}{\partial t} + \sigma E_\phi + J_\phi, \tag{5}$$

$$\frac{1}{\rho}\frac{\partial(\rho H_\phi)}{\partial \rho} - \frac{1}{\rho}\frac{\partial H_\rho}{\partial \phi} = \epsilon\frac{\partial E_z}{\partial t} + \sigma E_z + J_z. \tag{6}$$

In Eqs. $1-6$, the field components are functions of ρ, z, and ϕ. The coordinate system is shown in Fig. 3. Now, consider that the materials comprising the axially symmetric DCA are completely characterized in two dimensions by the parameters $\sigma(\rho, z)$, $\epsilon(\rho, z)$, and $\mu(\rho, z)$. In addition, we will require that the electromagnetic fields are composed of an infinite series of modes in $\cos m\phi$ and $\sin m\phi$, written succinctly as

$$E(\rho, z, \phi) = \sum_{m=0}^{\infty} E_c(\rho, z, m)\cos m\phi +$$
$$E_s(\rho, z, m)\sin m\phi \tag{7}$$

$$H(\rho, z, \phi) = \sum_{m=0}^{\infty} H_c(\rho, z, m)\cos m\phi +$$
$$H_s(\rho, z, m)\sin m\phi. \tag{8}$$

Substituting Eqs. 7 and 8 into Eqs. $1-6$, we find that $\frac{\partial}{\partial \phi}$ becomes $m\cos m\phi$ or $-m\sin m\phi$, and all of the $\cos m\phi$ or $\sin m\phi$ factors cancel, yielding

$$\mp\frac{m}{\rho}E_z - \frac{\partial E_\phi}{\partial z} = -\mu\frac{\partial H_\rho}{\partial t} - M_\rho, \tag{9}$$
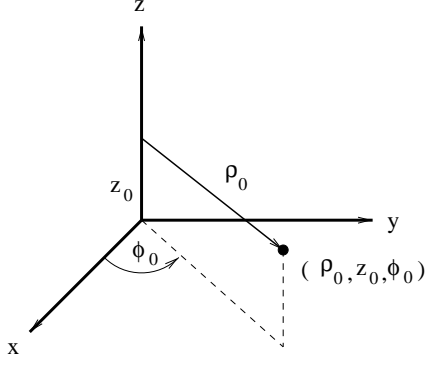
$$\frac{\partial E_\rho}{\partial z} - \frac{\partial E_z}{\partial \rho} = -\mu\frac{\partial H_\phi}{\partial t} - M_\phi, \tag{10}$$

$$\frac{1}{\rho}\frac{\partial(\rho E_\phi)}{\partial \rho} \pm \frac{m}{\rho}E_\rho = -\mu\frac{\partial H_z}{\partial t} - M_z, \tag{11}$$

$$\pm\frac{m}{\rho}H_z - \frac{\partial H_\phi}{\partial z} = \epsilon\frac{\partial E_\rho}{\partial t} + \sigma E_\rho + J_\rho, \tag{12}$$

$$\frac{\partial H_\rho}{\partial z} - \frac{\partial H_z}{\partial \rho} = \epsilon\frac{\partial E_\phi}{\partial t} + \sigma E_\phi + J_\phi, \tag{13}$$

$$\frac{1}{\rho}\frac{\partial(\rho H_\phi)}{\partial \rho} \mp \frac{m}{\rho}H_\rho = \epsilon\frac{\partial E_z}{\partial t} + \sigma E_z + J_z. \tag{14}$$

Figure 3: Cylindrical coordinate system.

The field components in Eqs. 9 – 14 are functions of ρ and z only, and may be solved in two dimensions. A stretched coordinate perfectly matched layer (PML) was used at the outer periphery of the FD-TD lattice to absorb outgoing waves. The PML formulation is identical to that described in [5] [6] [7]. Following these previous works, each field component must be split, resulting in a total of twelve equations which must be solved in the time domain. Choosing the upper sign and $m = 1$ in Eqs. 9 – 14, the six electric field equations are

$$A_\rho \epsilon \frac{\partial E_\rho^{(\phi)}}{\partial t} + (\Omega_\rho \epsilon + A_\rho \sigma) E_\rho^{(\phi)} + \Omega_\rho \sigma \int_{-\infty}^{t} E_\rho^{(\phi)}(\tau) d\tau$$
$$= m H_z - \rho J_\rho^{(\phi)}, \tag{15}$$

$$a_z \epsilon \frac{\partial E_\rho^{(z)}}{\partial t} + (\omega_z \epsilon + a_z \sigma) E_\rho^{(z)} + \omega_z \sigma \int_{-\infty}^{t} E_\rho^{(z)}(\tau) d\tau$$
$$= -\frac{\partial H_\phi}{\partial z} - J_\rho^{(z)}, \tag{16}$$

$$a_\rho \epsilon \frac{\partial E_\phi^{(\rho)}}{\partial t} + (\omega_\rho \epsilon + a_\rho \sigma) E_\phi^{(\rho)} + \omega_\rho \sigma \int_{-\infty}^{t} E_\phi^{(\rho)}(\tau) d\tau$$
$$= -\frac{\partial H_z}{\partial \rho} - J_\phi^{(z)}, \tag{17}$$

$$a_z \epsilon \frac{\partial E_\phi^{(z)}}{\partial t} + (\omega_z \epsilon + a_z \sigma) E_\phi^{(z)} + \omega_z \sigma \int_{-\infty}^{t} E_\phi^{(z)}(\tau) d\tau$$
$$= \frac{\partial H_\rho}{\partial z} - J_\phi^{(z)}, \tag{18}$$

$$a_\rho \epsilon \frac{\partial E_z^{(\rho)}}{\partial t} + (\omega_\rho \epsilon + a_\rho \sigma) E_z^{(\rho)} + \omega_\rho \sigma \int_{-\infty}^{t} E_z^{(\rho)}(\tau) d\tau$$
$$= \frac{\partial H_\phi}{\partial \rho} - J_z^{(\rho)}, \tag{19}$$

$$A_\rho \epsilon \frac{\partial E_z^{(\phi)}}{\partial t} + (\Omega_\rho \epsilon + A_\rho \sigma) E_z^{(\phi)} + \Omega_\rho \sigma \int_{-\infty}^{t} E_z^{(\phi)}(\tau) d\tau$$
$$= H_\phi - m H_\rho - \rho J_z^{(\phi)}. \tag{20}$$

The parameters A_ρ, $a_{\rho,z}$, and $\omega_{\rho,z}$ are the real and

imaginary variables associated with the stretched co-ordinate system. The six magnetic field equations may be derived in a similar manner. These equations are discretized in the normal fashion [8], with ϵ, μ, and σ defined for each two-dimensional cell, and with the electric and magnetic field components staggered in space by a half cell width, as shown in Fig. 4. The quantities $a_{\rho,z}$, $\omega_{\rho,z}$, and A_ρ are also staggered, consistent with the electric and magnetic field definitions. Each cell is assigned coordinates (i, j) in the computer code. This gridding scheme is identical to that in [9]. No special handling of the singularity at
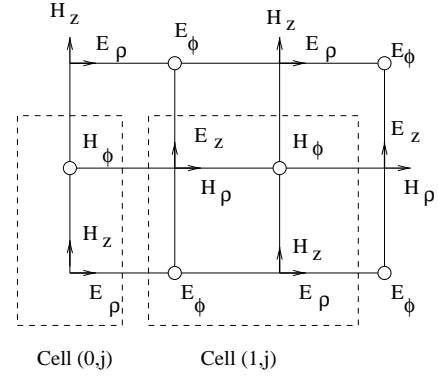
Figure 4: FD-TD lattice in cylindrical coordinates.

$\rho = 0$ ($i = 0$) is required when $m = 1$. Note that H_z is zero at $\rho = 0$ when $m = 1$, and need not be updated in the FD-TD computer code. In addition, H_ϕ and E_ρ are not needed to compute the other field components elsewhere in the lattice for $i \geq 1$. Thus, these three field components are not stored in the FD-TD code for cells located at $(0, j)$.

A ten cell thick fourth order tapered profile for ω_ρ and ω_z is placed at the edges of the lattice. Throughout the lattice, a_ρ and a_z were set to 1.0. Since $a_{\rho,z}$ and $\omega_{\rho,z}$ in Eqs. 15 – 20 behave very much like ϵ_r and σ/ϵ, respectively, the maximum value for ω was chosen in accordance with

$$\omega_{max} = \frac{\sigma_{max}}{\epsilon} = \frac{n+1}{150\pi \Delta a_{max} \epsilon_0}, \tag{21}$$

which is based on the classic optimum choice for σ_{max} in Cartesian coordinates [10]. In Eq. 21, n is the polynomial order of the profile ($n = 4$) and Δ is the cell size. Since $a_{\rho,z}$ is 1.0 throughout the lattice, a_{max} is 1.0 in our case.

3.1. Source Considerations

It is well known that a rectangular microstrip patch antenna operating in the fundamental mode may be approximately modeled by two-dimensional linear magnetic current sources located at the effective

edges of the patch element. In accordance with the cavity model, the strength of the magnetic current is determined by E_z at the effective edges of the patch element, shown as small arrows in Fig. 5 [11]. This concept also applies to circular patch antennas.
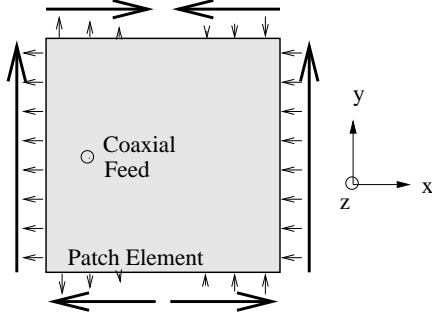
Figure 5: Rectangular microstrip patch antenna model.

However, for the circular patch, the magnetic current would of course obey a $\cos\phi$ variation. A top view of the circular patch model is shown in Fig. 6. The thickness of the arrows is meant to represent the magnitude of the magnetic current. The source antenna
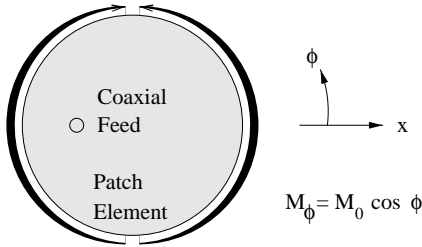
Figure 6: Circular microstrip patch antenna model.

used on the DCA is a small rectangular patch approximately 2 cm square. In cylindrical coordinates, the linear magnetic currents associated with the rectangular patch, shown in Fig. 5 are difficult to model exactly. One could model the square patch by synthesizing a series azimuthal modes, using multiple terms in Eqs. 7 and 8. However, the FD-TD code would need to be executed for each desired mode. For the purposes of this analysis, we chose to use only the first azimuthal harmonic ($m = 1$) to model the square patch antenna. This, means of course, that we are actually modeling a circular patch, as shown in Fig. 6. To first order, the behavior of the rectangular patch and the DCA will be adequately modeled by the approximate source.

To activate the source numerically, we employ a soft source at a single cell location (ρ_0, z_0). To achieve

right-hand circular polarization (RHCP), one would simply include an additional $\sin\phi$ source which is fed 90° out of phase with the $\cos\phi$ source. This compound source is expressed analytically as

$$M_\phi(\rho, z) = M_0(\rho_0, z_0) \cdot (\cos\phi - j\sin\phi). \qquad (22)$$

To implement the $\cos\phi$ and $\sin\phi$ sources, one would need to, in theory, run the FD-TD code twice, with each run separately using the upper and lower signs in Eqs. 9 – 14. However, we chose to simply run the code once with a $\cos\phi$ oriented source. We then computed the radiation patterns in the $\phi = 0°$ and $\phi = 90°$ planes (E and H-planes, respectively). Recognizing the spatial orthogonality of the $\cos\phi$ and $\sin\phi$ functions, we then phase shift the H-plane pattern by $-90°$, and add it to the E-plane pattern, thus yielding the RHCP pattern.

4. Numerical Results

The FD-TD code was run for three different types of antennas: a Trimble microstrip patch mounted on a 30 cm diameter aluminum plate, a Novatel 501 antenna mounted on a choke ring ground plane, and finally, the DCA. In all cases, the cell size was $\lambda_0/200$ square, and the time step Δt was set to 70% of the maximum Δt allowed for stability [12],

$$\Delta t = \frac{0.7}{c}\frac{\Delta}{\sqrt{2}}, \qquad (23)$$

where $\Delta = \Delta\rho = \Delta z$. Steady state conditions were reached after 10,000 time steps. Plots of the theoretical radiation patterns for each case are shown in Figs. 7, 8, and 9. The dielectric material assumed
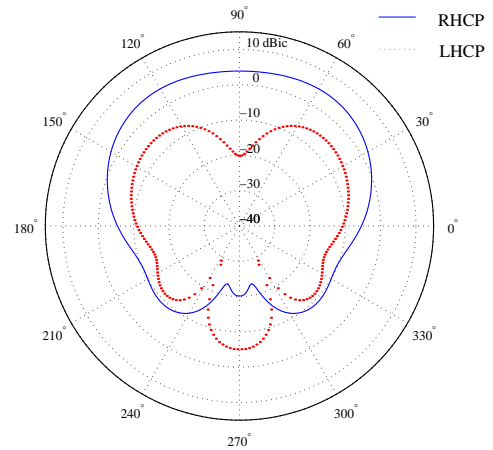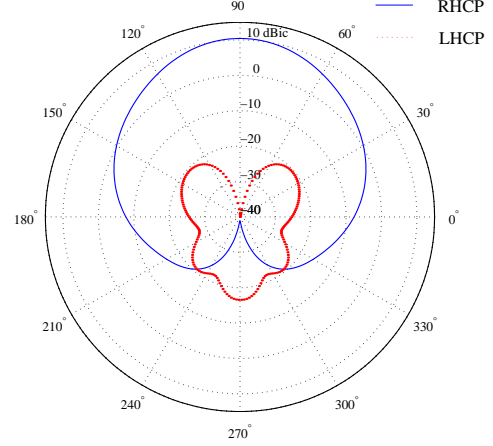

Figure 7: Theoretical radiation pattern of Trimble patch antenna mounted on 30 cm diameter plate.

in the cavity of the DCA is polyethylene, for which $\epsilon_r = 2.37$. Polyethylene is inexpensive, readily available, and has low loss ($\tan\delta = 70$ μrad at 1.575 GHz) [13]. The cavity depth was chosen to be 4.08 cm, which is optimum for $\epsilon_r = 2.37$. The radial length of the cavity is taken to be 9.3 cm. This value was arrived at after starting at the ideally optimum value of 7.5 cm from Fig. 2, then running the FD-TD code many times and adjusting the length until the desired radiation pattern was achieved. Comparing
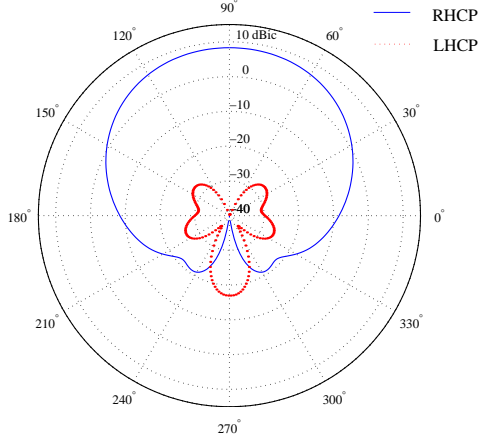

Figure 8: Theoretical radiation pattern of Novatel 501 mounted on choke ring ground plane.

Figs. 8 and 9, we find that the DCA performs nearly as well as the choke ring with regard to cross polarization rejection, and sensitivity to satellites in the upper hemisphere. Both the choke ring and DCA are more resistant to interferers or multipath from below the horizon, when compared to the simple circular ground plane in Fig. 7. One advantage of running an FD-TD analysis is that all six field components are known in the vicinity of the antenna structure. Figs. 10 and 11 show the magnitude of the transverse magnetic field (H_ϕ) in the near-field of the Novatel choke ring antenna and DCA, respectively. Notice that H_ϕ is minimized at the top surface of the corrugations in Fig. 10, and along the top surface of the cavity in Fig. 11. This confirms that the corrugations and the cavity are acting as artificially soft surfaces. In addition, one observes that the field structure within the corrugations in Fig. 10 is primarily TEM, *i.e.*, there is essentially no field variation in the ρ direction within the corrugations. Within the cavity of the DCA, H_ϕ exhibits a $\cos k_\rho\rho \cdot \cos k_z z$ behavior, as expected for a cavity at resonance. These types of figures can be produced for each of the six field components. The figures highlight the usefulness of the FD-TD method for providing valuable insight into the electromagnetic behavior of antenna systems.


**Figure 9:** Theoretical radiation pattern of DCA Prototype.
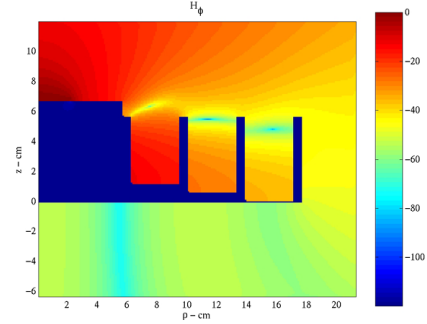
Figure 10: Near-field components of Novatel choke ring.

5. Experimental Results

A prototype DCA was built with polyethylene as the cavity dielectric material, and aluminum as the structural material. A photograph of the prototype DCA is shown in Fig. 12. The aluminum structure was machined from a cylindrical slab of metal. The polyethylene is provided by the manufacturer in the form of 3 mm diameter pellets. These pellets were melted into a cylindrically shaped slab, allowed to cool, and then machined to fit within the cavity of the aluminum structure. A 2 cm square microstrip patch antenna (Toko DAK1575MS50) was used as the radiating element. The DCA was placed on the roof of a tall building on Stanford campus. A low noise pre-amplifier (LNA) was built and placed at the antenna feed point. Approximately 100 meters of coaxial cable runs from the roof to the lab below, where the coax was connected to a GPS receiver. The receiver was set to track one satellite (PRN 29) over
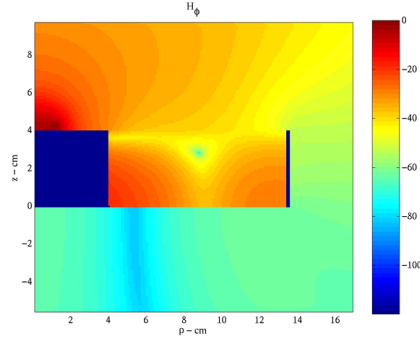
Figure 11: Near-field components of optimized DCA.
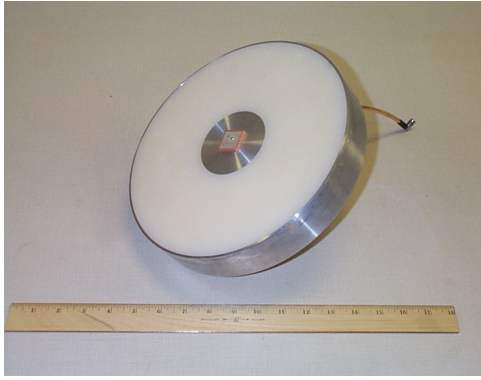

Figure 12: Prototype DCA.

the course of three consecutive days. The satellite position (azimuth and elevation) and signal-to-noise ratio (SNR) were recorded for each of the three antennas on a different day. The raw SNR data will not yield the actual radiation pattern of the antenna *v.s.* elevation angle. Errors due to multipath, tropospheric loss, change in satellite range, and the GPS satellite antenna pattern all contribute to the error in the received SNR. These effects become more pronounced near the horizon. To determine the actual radiation pattern, the measured radiation pattern of the Novatel choke ring was compared to the known radiation pattern, provided by Novatel [14]. The difference between the known and measured patterns is taken to be the total error due to these effects, and is shown in Fig. 13. This error function is subtracted from the raw measured data, yielding a best estimate of the actual radiation pattern. The error function will vary for different antenna sites, and for each particular satellite and its path in the sky. Since all measurements were taken at the same location from the same satellite on three consecutive days, it is assumed that this error function is applicable to all three data
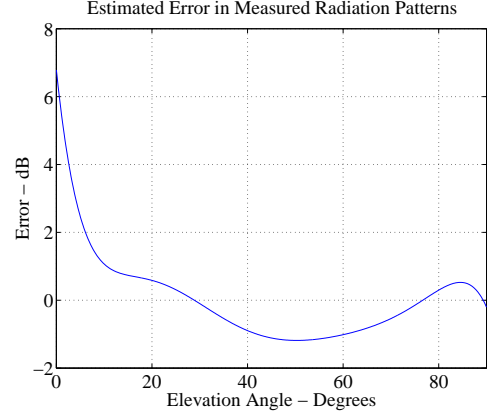
**Figure 13:** Function used to calibrate errors out of the measured data.

sets.

In Figs. 14, 15, and 16, the measured radiation patterns are compared to the patterns obtained from the FD-TD analysis. Since SNR measurements were not
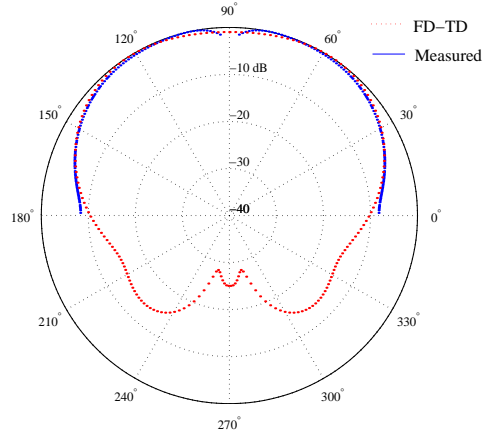

Figure 14: Radiation pattern of Trimble patch antenna mounted on 30 cm diameter plate.

available from below the horizon, it was not possible to estimate the gain of the antennas. Thus, the experimental data are normalized to the peak SNR, which is taken to be 0 dB. The measured choke ring and circular ground plane antenna patterns match the theoretical patterns well, to within 1.5 dB over the hemisphere. However, the theoretical DCA pattern using a dielectric having $\epsilon_r = 2.37$ does not match the experimental results. The reason for this is that during the dielectric melting and cooling process, pockets of air became trapped in the dielectric. These pockets were plugged with dielectric slugs as much as pos-
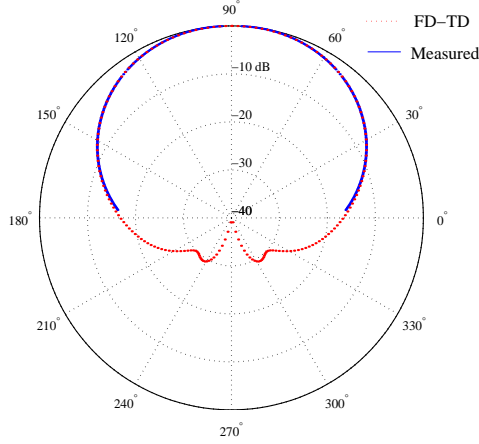
Figure 15: Radiation pattern of Novatel 501 mounted on choke ring ground plane.
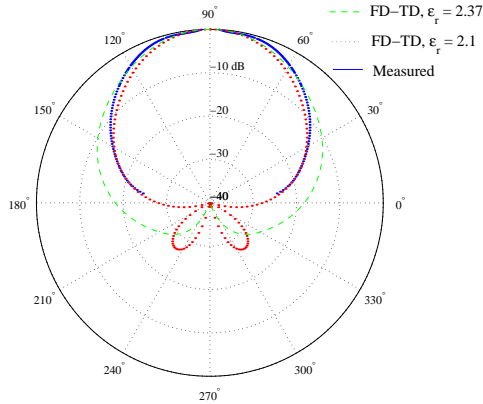
Figure 16: Radiation pattern of DCA Prototype.

sible, but it is evident that some air still remained trapped in the dielectric cavity. Shown also in Fig. 16 is a DCA radiation pattern using a dielectric having $\epsilon_r = 2.1$. This pattern matches the experimental data well, and we infer from this that the air pockets in the polyethylene have lowered the effective permittivity of the material from 2.37 to 2.1.

Although the prototype DCA is insensitive to interference and multipath originating from below the horizon, GPS satellite signals arriving from below 45° elevation are severely attenuated by the antenna, and the measured SNR is consequently quite low at these elevation angles. In fact, PRN 29 was lost by the receiver at 11° elevation, while the choke ring allowed the receiver to track PRN 29 to 4° elevation. The ground plane antenna permitted tracking down to the horizon. Of course, if the relative permittivity of the DCA's cavity were actually 2.37, its performance

would be more in line with the choke ring. This being true, the DCA would still provide poor reception of low elevation satellites, and is not an ideal general purpose interference resistant aircraft antenna. Such an antenna could, however, be useful in the event that interference is detected, and threatens or prevents airborne GPS navigation. The DCA could be used as a contingency antenna to provide minimal coverage of high elevation GPS satellites, while rejecting the ground based interference.

6. An Airworthy DCA

The prototype DCA is large and heavy, and thus ill suited for airborne applications. However, when high-permittivity dielectrics are used in the cavity, the size of the cavity is reduced in accordance with Fig. 2. We have analyzed a DCA with a cavity having $\epsilon_r = 20$. This antenna is only 1 cm tall, and 18 cm in diameter. In comparison, the Trimble airborne patch antenna is 2 cm tall and 13 cm wide, along its diagonal. So the idea of building a DCA small enough for airborne applications is reasonable.

7. Conclusions

This paper described the analysis, design, and testing of an interesting type of interference resistant GPS antenna. The DCA uses a dielectric cavity as an artificially soft surface to attenuate signals arriving from below the antenna. The antenna is analyzed by an efficient 2.5-dimensional FD-TD algorithm, whereby the axial symmetry of the DCA is used to reduce a potentially full three-dimensional analysis to a two-dimensional analysis. Modeling the DCA's rectangular patch antenna by a circumferential magnetic line current is not likely to significantly affect the accuracy of the analysis. The DCA is shown to perform similarly to the choke ring antenna. Smaller models of the DCA may be built, using high permittivity dielectric materials.

8. Acknowledgments

and sacrificed personal time to assist in the machining and fabrication of the DCA. The authors also acknowledge the generosity of the Union Carbide Corporation with regard to the free samples of dielectric material used for the prototype DCA. The technical assistance and advice of David Frankowski of Union Carbide were very much appreciated, as well as his patience in dealing with our repeated attempts at fabricating the prototype. Finally, thanks to Sasha Mitelman for proofreading this paper and providing useful comments.

References

[1] A. Taflove. *Computational Electrodynamics: The Finite Difference Time Domain Method*. Artech House, Boston, MA, 1995.

[2] P-S. Kildal. Artificially soft and hard surfaces in electromagnetics. *IEEE Transactions on Antennas and Propagation*, AP-38(10):1537 – 1544, October 1990.

[3] M. Leoncini L. Borselli S. Maci, S. Raffaelli and P-S. Kildal. Analysis of surface-wave excitation and radiation mechanisms of a monopole on a circular grounded dielectric slab with critical thickness. *IEE Proceedings on Microwaves, Antennas and Propagation*, 143(4):335 – 340, August 1996.

[4] P-S. Kildal Z. Ying and A. A. Kishk. Study of different realizations and calculation models for soft surfaces by using a vertical monopole on a soft disk as a test bed. *IEEE Transactions on Antennas and Propagation*, AP-44(11):1474 – 1481, November 1996.

[5] F. L. Teixeira and W. C. Chew. PML-FDTD in cylindrical and spherical grids. *IEEE Microwave and Guided Wave Letters*, 7(9):285 – 287, September 1997.

[6] F. L. Teixeira and W. C. Chew. Finite-difference computation of transient electromagnetic waves for cylindrical geometries in complex media. *IEEE Transactions on Geoscience and Remote Sensing*, 38(4):1530 – 1543, July 2000.

[7] F. L. Teixeira and W. C. Chew. A nonuniform cylindrical FDTD algorithm with improved PML and quasi-PML absorbing boundary conditions. *IEEE Transactions on Geoscience and Remote Sensing*, 37(2):1066 – 1072, March 1999.

[8] K. S. Yee. Numerical solution of initial boundary value problems involving Maxwell's equations in isotropic media. *IEEE Transactions on Antennas and Propagation*, AP-14(3):302 – 307, May 1966.

[9] R. Mittra Y. Chen and P. Harms. Finite-difference time-domain algorithm for solving Maxwell's equations in rotationally symmetric geometries. *IEEE Transactions on Microwave Theory and Techniques*, MTT-44(6):832 – 839, June 1996.

[10] S. D. Gedney. An anisotropic perfectly matched layer-absorbing medium for the truncation of FDTD lattices. *IEEE Transactions on Antennas and Propagation*, AP-44(12):1630 – 1639, December 1996.

[11] A. G. Derneryd. Linearly polarized microstrip antennas. *IEEE Transactions on Antennas and Propagation*, AP-24(6):846 – 851, November 1976.

[12] M. Fusco. FDTD algorithm in curvilinear coordinates. *IEEE Transactions on Antennas and Propagation*, AP-38(1):76 – 89, January 1990.

[13] Union Carbide Corporation D. J. Frankowski. *Personal Communication*. 30 August 2000.

[14] Novatel Corporation R. Faulkner. *Personal Communication*. 31 August 2000.